Variability of Near-Surface Currents Observed during the Pole Experiment

RUSS DAVIS, T. P. BARNETT AND C. S. COX

University of California, San Diego, and Scripps Institution of Oceanography, La Jolla 92093

(Manuscript received 9 November 1976, in final form 4 November 1977)

ABSTRACT

Variability of near-surface currents over a 20-day period in a 150 km diameter region of the central North Pacific is described using vertical profiles from a current meter and the tracks of 25 drifting buoys. Energetic fluctuations of order 0.10 m s^{-1} having time scales of a few days and vertical scales in excess of 100 m were found, apparently coherent with the wind forcing. Buoy tracks disclose a small-scale (<15 km) short-period (less than a few days) variability with speeds of the order 0.05 m s^{-1} and an energetic mesoscale motion with speeds of the order 0.07 m s^{-1}, space scales of the order 40 km and time scales exceeding 20 days. Additionally, the difference between the mean current observed over the experiment, having a speed of about 0.03 m s^{-1}, and the climatological norm inferred from ship-drift, with a speed of about 0.10 m s^{-1}, suggests a larger scale variability not adequately resolved.

1. Introduction

One of the objectives of the North Pacific Experiment (NORPAX) is to describe the structure and dynamics of near-surface thermal anomalies having time scales of months and horizontal dimensions of order 1000 km. These anomalies, first identified in surface temperature (e.g., Namias, 1970), are believed to penetrate at least to the depth of the mixed layer (White and Walker, 1974; Barnett, 1976).

Lateral advection is one factor likely to contribute to the development of near-surface anomalies. The standard deviation of one-month anomalies of surface temperature are typically 1°C (Davis, 1976); an anomalous current of 0.02 m s^{-1} across a climatological normal mean horizontal temperature gradient of order 1°C (100 km)$^{-1}$ will produce such a temperature anomaly in less than two months. Anomalous currents of this magnitude could result from changes of the oceanic general circulation or superficial responses to surface wind stress changes (a change of 30% of the mean wind stress would produce the required Ekman drift in a 25 m momentum mixed layer throughout most of the central Pacific).

The POLE Experiment was conceived as a first step toward gathering the basic information required to design an experimental plan for quantitative investigation of the mechanisms of thermal anomaly development. One element of the required information is an understanding of the types of motion potentially contributing to advection. Another is knowledge of the space and time scales of motions smaller than the anomalies of interest since these motions are the noise which must be filtered out in resolving anomaly scale currents. See Bretherton *et al.* (1976) for a discussion of how such scale information is used to optimize the tradeoff between accuracy, resolution and area of coverage in the design of oceanographic sampling networks.

The purpose of this paper is to describe the structure and scale information of near-surface currents observed during POLE. The experiment was conducted in January and February of 1974 and was centered at 35°N, 155°W. The time and location were chosen in hopes of observing upper ocean response to wind forcing from storms, but none was encountered. Information on the temporal and vertical structure of currents was obtained from a current meter profiling the upper 135 m from the spar buoy *Flip*. Horizontal structure, over scales from 10 to 100 km, was deduced from 25 drogued drifting buoys. The 21-day duration of observations was too short to provide information on the anomaly time scale but did resolve an energetic upper layer mesoscale variability which, if usually present, will make difficult quantitative measurement of anomaly scale near surface currents. The variability is interesting in its own right and does not seem to correspond to any previously described type of motion. It is hoped that when the velocity observations are combined with temperature and density measurements, it will be possible to more fully describe this mesoscale variability.

The current meter profiling results are described in section 2 and the drifter results in section 3. Some thoughts on the implications of these results to sampling strategies for observing large-scale currents are given in section 4. The technical details of the observing systems are given in Appendices.

0022-3670/78/0290-0301$06.00
© 1978 American Meteorological Society

Unauthenticated | Downloaded 06/20/24 10:10 PM UTC

2. Current meter profiling

A propeller-type current meter (described in Appendix A) was profiled from *Flip* which was freely drifting within a few kilometers of 35°N, 155°W. *Flip*'s position was determined from satellite fixes and a record of the drift velocity was computed by optimal interpolation (see Appendix A). The profiling procedure consisted of occupying one of the depths 3, 6, 9, 12, 18, 30, 45, ···, 120, 135 m for a period of 3–15 min. All levels were not occupied in sequence; rather, the sampling scheme was varied to allow a rich sampling of time separations between various levels. In normal practice the 135 m depth range was covered in 90 to 150 min.

The basic current meter data was a record of 10 s mean velocities made by averaging 2 s readings. The current meter velocities (velocity relative to *Flip*) were added to the drift velocity record to obtain an absolute velocity. The relative and drift velocities were comparable (0.12 m s^{-1} rms). Because high-frequency drift motions could not be resolved, the drift record has little energy above 1 cycle per hour (cph). The variance of 10 s average relative velocities was approximately twice that of the record constructed by averaging over the periods during which the meter was held at one level (typically 10 min).

The temporal and vertical structure of currents and wind stress were described using rotary spectral analysis (Gonella, 1972). In synopsis, this consists of representing a horizontal vector (such as current velocity **u** or wind stress τ) in the complex form

$$u_x + iu_y \equiv U = \sum_{f=-\infty}^{\infty} A_U(f) \exp(2\pi i f t) \quad (2.1)$$

so that positive (negative) frequencies represent components whose direction rotates counterclockwise (clockwise) when viewed from above. The rotary cross spectrum of two vectors **u** and **v** is

$$R_{UV}(f) = <A_U(f)A_V^*(f)>/\Delta f, \quad (2.2)$$

where the asterisk is the complex conjugate and Δf the frequency interval in (2.1). The phase of the rotary cross spectrum is the typical angle between the components of **u** and **v** having frequencies f. The rotary coherence is defined, analogous to the scalar coherence, by

$$C_{UV} = |R_{UV}|/[R_{UU} \cdot R_{VV}]^{1/2}. \quad (2.3)$$

The scalar spectrum, normalized so that

$$\int_{-\infty}^{\infty} S_{UU}(f)df = \langle |\mathbf{u}|^2 \rangle,$$

where f is the cyclic frequency, is related to R by

$$S_{UU}(f) = \tfrac{1}{2}[R_{UU}(f) + R_{UU}(-f)].$$

The rotary autospectra were estimated from the lagged mean products of u_x and u_y computed at each level occupied during profiling. The range of time lags was 10 s to 160 h. These mean lagged products were averaged over the three depth ranges 3–30 m, 30–90 m and 90–150 m. No asymmetry of the rotary spectra was observed at frequencies >1 cph so the conventional spectrum was used to describe the high frequencies. A similar analysis was applied to wind stress except that the mean-lagged product was computed only for lags ≥1 h. The resulting spectra for the 3–30 m and 90–150 m ranges and for the wind stress are shown in Figs. 1 and 2. The current velocity spectrum for the 30–90 m depth range is similar to the two shown and falls approximately midway between them on a logarithmic scale. The straight lines in Fig. 1 correspond to $S(f) = (0.002$ m^2 $s^{-2})f^{-1}$ and are intended primarily to aid comparison of the two spectra. The number of degrees of freedom increases with frequency, being roughly 500 f/(cph) in both the current and wind spectra.

The following observations may be made from the autospectra:

1) The peaks around 0.05 cph in the clockwise (negative frequency) rotary spectra of currents are almost certainly inertial currents. The peaks are not large; inertial motions are evident in the current records but do not dominate them. No inertial peak is found in the wind spectrum.

2) Both current and wind spectra show more energy at low frequencies in clockwise rotary motion than in counterclockwise. The discrepancy is, however, considerably more marked in the wind.

3) The wind spectrum has a considerably more rapid decrease with frequency than do the current spectra. In particular, the current spectra decay slowly, approximately as f^{-1}, for frequencies below 10 cph.

4) There is significantly more energy in high frequency (>10 cph) variability in shallow water than at depth. This is not due to the decay of surface wave motions with depth since these would have frequencies above 150 cph. The small peaks around 80 cph are most likely the result of near resonant tilting motions of *Flip*.

An adequate description of the variability observed during POLE can only be gained by examining time series of the wind stress and currents at various depths. The relatively slow decay of the current autospectra with frequency means that the time series of currents at individual depths are significantly aliased and that the sampling scheme oversampled in the vertical and undersampled in time. To alleviate this, records from neighboring levels were taken as samples of the velocity in depth ranges. Records were thus combined to form time series for the ranges 3–9, 12–18, 30–45, 60–75,

Unauthenticated | Downloaded 06/20/24 10:10 PM UTC

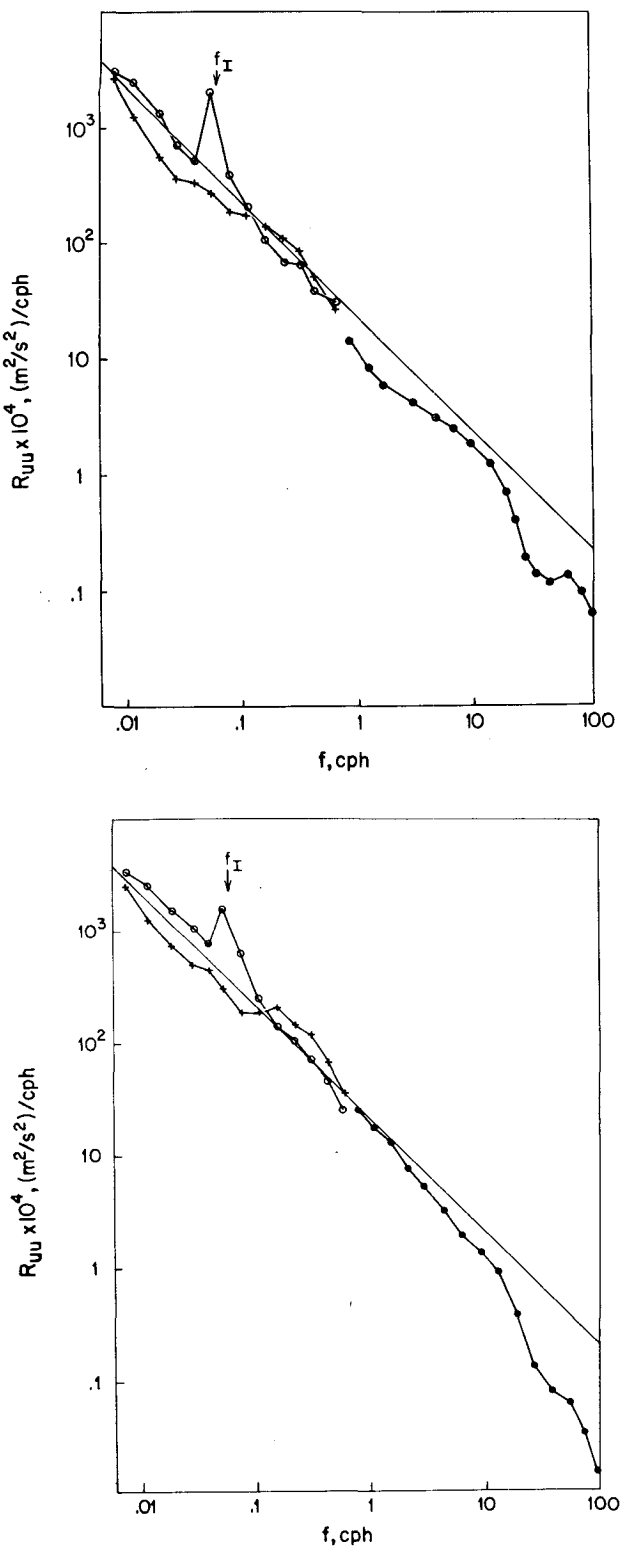

FIG. 1. Frequency spectrum of currents in the depth range 3–30 m(a) and 90–150 m(b). Rotary spectral analysis is used for the lower frequencies with open circles for negative (clockwise) frequencies, and +'s for positive frequencies. The inertial frequency is denoted by f_I and the straight line corresponds to the spectrum of $(0.002\ m^2\ s^{-2})/f$.

90–105 and 120–135 m. These records were still poorly sampled in time (there is typically 90 to 150 min between samples in these composite records) so only low-frequency components can be investigated. Consequently, records of 10 h averages, sampled every 5 h, were formed by averaging with equal weight the mean currents in each depth range obtained from the profiles falling in the appropriate time periods.

A qualitative picture of the vertical structure of currents and their relation to the wind stress can be obtained from Fig. 3, a "stick" plot of 20 h averages of wind stress and current velocity. Additional vertical smoothing has been done in this figure by averaging over the four depth ranges shown. A marked similarity of currents at different levels is evident and the eye suggests that the currents are coherent with, and approximately parallel to the wind stress.

A more quantitative description of vertical and temporal structure, and the relation between wind and currents can be gained by rotary cross-spectral analysis. Such analysis was accomplished by computing the Fourier amplitudes A of (2.1) from two overlapping 320 h blocks of the records for the six current depth ranges and the wind stress. The rotary cross spectra R of (2.2) were obtained by averaging over the two blocks and over three neighboring frequency bands; thus the number of degrees of freedom is approximately the same as if four complex numbers had been averaged.

Fig. 4 is a contour plot of the rotary coherence C of (2.3) and the phase of the rotary cross spectrum between currents in the shallowest depth range, 3–9 m, and those in deeper ranges. Fig. 5 is a similar plot for the cross spectrum between wind stress and currents in various depth levels. In preparing these plots, vertical smoothing was accomplished by applying a two-depth running mean filter. Thus the equivalent number of degrees of freedom is approximately 16. Following Jenkins and Watts (1968), the estimated coherence would be less than 0.4 with 90% confidence if the series are uncorrelated and the spectra white, and the 90% confidence limits on the phase would be approximately $\pm 18°$ when the true coherence if 0.7 and greater when the coherence is less. The spectra are far from white so the true significances are considerably less than this would suggest. As a consequence, coherences of less than 0.5 were deemed insignificant and the associated phases are not shown in Figs. 4 and 5.

The following observations may be made from Figs. 3–5:

5) The vertical coherence of currents is significant from $f \approx -0.08$ to $f \approx 0.02$ cph. The lowest frequency components are highly coherent and essentially parallel over the entire depth range. The

Unauthenticated | Downloaded 06/20/24 10:10 PM UTC

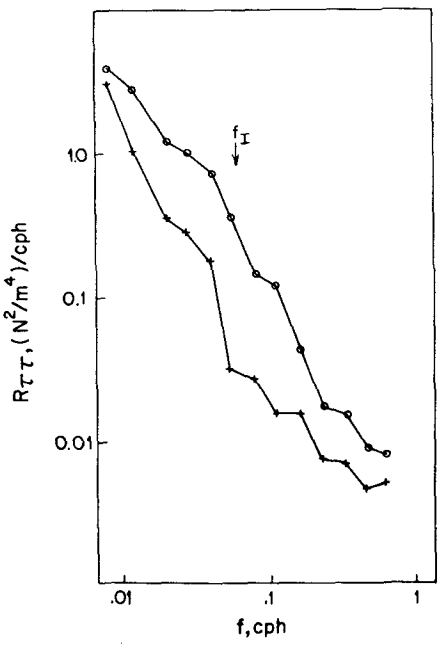

FIG. 2. Rotary frequency spectrum of the wind stress. Symbols as in Fig. 3.

tendency for components with $f \approx -0.04$ to veer to the right with depth while those with $f \approx -0.07$ veer to the left may be significant.

6) The coherence between wind stress and currents is lower than between currents at different levels. The phase differences are within the confidence limits of zero degrees; the data cannot be used to disprove the hypothesis that wind and wind-driven current are parallel.

Can the observed current and wind relations be reconciled with Ekman layer, or local wind forcing, dynamics? Consider the model equations

$$\partial_t(u_1,u_2) + 2\pi f_I(-u_2,u_1) = \partial_z(\sigma_1,\sigma_2), \quad (2.4)$$

where f_I is twice the cyclic frequency of the local rotation rate (the f plane approximation), $\boldsymbol{\sigma}$ is the turbulent Reynolds shear stress acting on a horizontal surface normalized by density, and all effects of horizontal variation are neglected. Relating $\boldsymbol{\sigma}$ to the velocity $\mathbf{u}$ and the density-normalized wind stress $\boldsymbol{\tau}$ is a fundamental and unsolved problem in the study of the ocean's upper layers. However, a model-independent relation between the wind-

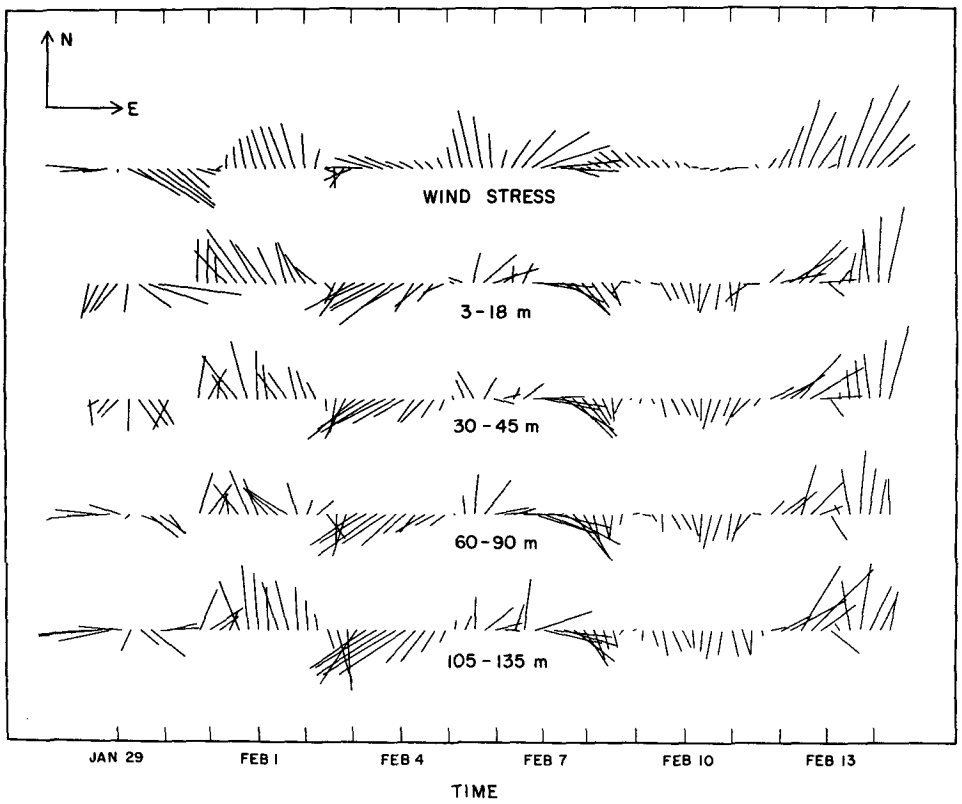

FIG. 3. Vector plot of wind stress (upper) and velocity in the depth ranges shown. Vectors represent 20 h averages and are plotted every 5 h. The vectors in upper left corner show true headings and are of a length corresponding to 0.02 N m^{-2} (2 dyn cm^{-2}) and 0.2 m s^{-1}.

Unauthenticated | Downloaded 06/20/24 10:10 PM UTC

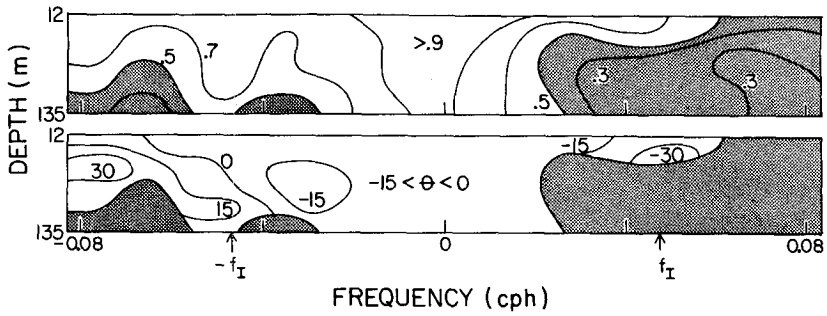

FIG. 4. Contour plot of rotary coherence (upper panel) and rotary phase (lower) of currents at various depths with currents in the depth range 3–9 m. Coherence below 0.5 is deemed insignificant so that phases are not shown. Convention is such that a positive phase corresponds to deeper current to the left of surface current. The inertial frequency is f_I.

driven transport **Q** and surface stress can be gained by integrating from below the layer where σ is significant to the surface. In terms of the rotary coefficients A of (2.1) this relation is

$$A_Q(f) = \frac{-i}{2\pi(f + f_I)} A_\tau(f). \tag{2.5}$$

For rotary frequencies $> -f_I$ the transport is to the right of the stress, at $f = -f_I$ inertial motions are resonantly excited so the response cannot be computed from this simple model, and for f more negative than $-f_I$ the transport is to the left of the stress. The rotary cross-spectral relations corresponding to (2.5) are

$$R_{QQ} = [2\pi(f + f_I)]^{-2} R_{\tau\tau}, \tag{2.6a}$$

$$R_{Q\tau} = -i[2\pi(f + f_I)]^{-1} R_{\tau\tau}. \tag{2.6b}$$

The first test which can be applied is a comparison of the energy of observed currents and that expected from wind forcing by the observed stress. Toward this end, $R_{Q\tau}$ was computed for transport **Q** over various depth ranges and compared with (2.6b). This showed that the transport which appears from the cross-spectral analysis to be related to the wind is much larger, generally by a factor of 5, than predicted. Both the transports above and below 60 m (well below the depth of momentum transfer expected from the weak observed winds) were larger than the total transport expected from Ekman theory. A second discrepancy with Ekman theory is evident from the phases of $R_{u\tau}$ shown in Fig. 5 and is confirmed from the calculations of $R_{Q\tau}$; in contrast to theory the apparently wind-driven transport is parallel to the wind stress rather than being to the right for $f > -f_I$ and to the left for $f < -f_I$. In retrospect this latter finding is not surprising in view of the first discrepancy; if the apparently wind driven variability is too large to be generated by the local wind, there is no reason to expect it to have any particular phase relation with the local wind. Hence we make the final observation.

7) Most of the current variability which appears coherent with the wind is not generated by local wind.

3. Drifting buoy results

A qualitative picture of drifter results is given in Fig. 6. These illustrations were constructed by linearly interpolating the positions of individual

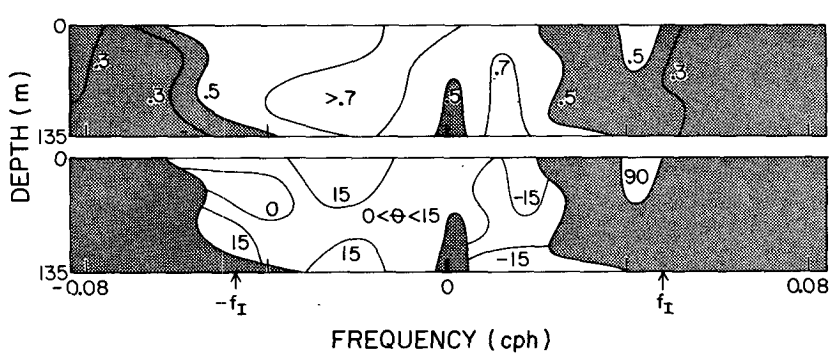

FIG. 5. As in Fig. 4 except for currents at various depths with wind stress. A positive phase corresponds to velocity component to the left of stress component.

Unauthenticated | Downloaded 06/20/24 10:10 PM UTC

buoys drogued at 30 m to obtain positions at 100 h intervals. The 100 h pseudo-observation times were generally close to actual observations so the interpolation did not greatly influence the buoy positions. Regularizing the observation intervals allows plotting buoy positions so that displacements of position are proportional to the time average buoy velocity. Buoy motion over three overlapping 200 h periods are shown.

Several distinct regions are evident in the flow field. On the western side of the area most of the buoys initially move toward the northwest, later turning to the north. Speeds of the order 0.1 m s^{-1} are common among this group. The three buoys in the northeast quadrant partake in a confused circulation that moves them slowly (<0.05 m s^{-1}) westward. Even though the three buoys are separated by only 10 km, their velocities differ greatly: two move west while the one between them moves east. A third group of buoys in the southeast region moves at an accelerating pace toward the southeast. The flow in the POLE area is complex in its horizontal character. The overall picture of the buoy drifts is one of a general straining motion that elongates the initial, essentially circular, distribution in the northwest–southeast directions.

The horizontal and temporal scales of surface currents in POLE were characterized in terms of the structure function

$$D(r,\tau) = \left\langle \left|\mathbf{u}(\mathbf{x}_1,t_1) - \mathbf{u}(\mathbf{x}_2,t_2)\right|^2 \right\rangle, \qquad (3.1)$$

where the average is taken over all observation pair with $r - \delta r/2 \leq |\mathbf{x}_1 - \mathbf{x}_2| < r + \delta r/2$ and $\tau - \delta\tau/2 \leq |t_2 - t_1| < \tau + \delta\tau/2$. Using $\delta\tau$ of 100 h and δr of 20 km provided between 50–200 estimates of D in each lag bin. The velocities $\mathbf{u}(\mathbf{x},t)$ were those evaluated from two successive buoy positions (Fig. 6) and assigned the mid-point position and time.

Selected "cuts" of D through the sample space are shown in Fig. 7. They suggest the following conclusions:

1) Even for buoys with simultaneously determined velocities and spatial separations on the order of 10 km, the rms velocity difference is of the order 0.07 m s^{-1}. This is approximately 10 times larger than the errors associated with positioning. We conclude that this variability is real and is due to motions with either space or time scales too small to be resolved by the sampling network.

2) The slow increase with τ of $D(r,\tau)$ indicates that all resolved space scales were nearly stationary. The lack of structure in τ-space suggests uniform, weak time changes and hence a time scale that is large compared with the sampling durations.

3) $D(r,\tau)$ shows a rapid increase from r = 10 km to r = 50 km as well as a significant rise as r increases further for all values of τ (only two examples are shown in Fig. 7). This indicates the existence of a richness of space scales in the velocity field. The rapid increase in D at small r for all τ indicates energetic motions with long time scales (too long to be resolved) and space scales of the order 40 km. The increase at larger spatial scales discloses a low-frequency variability with space scales too large to be resolved in the experiment. It is this scale which

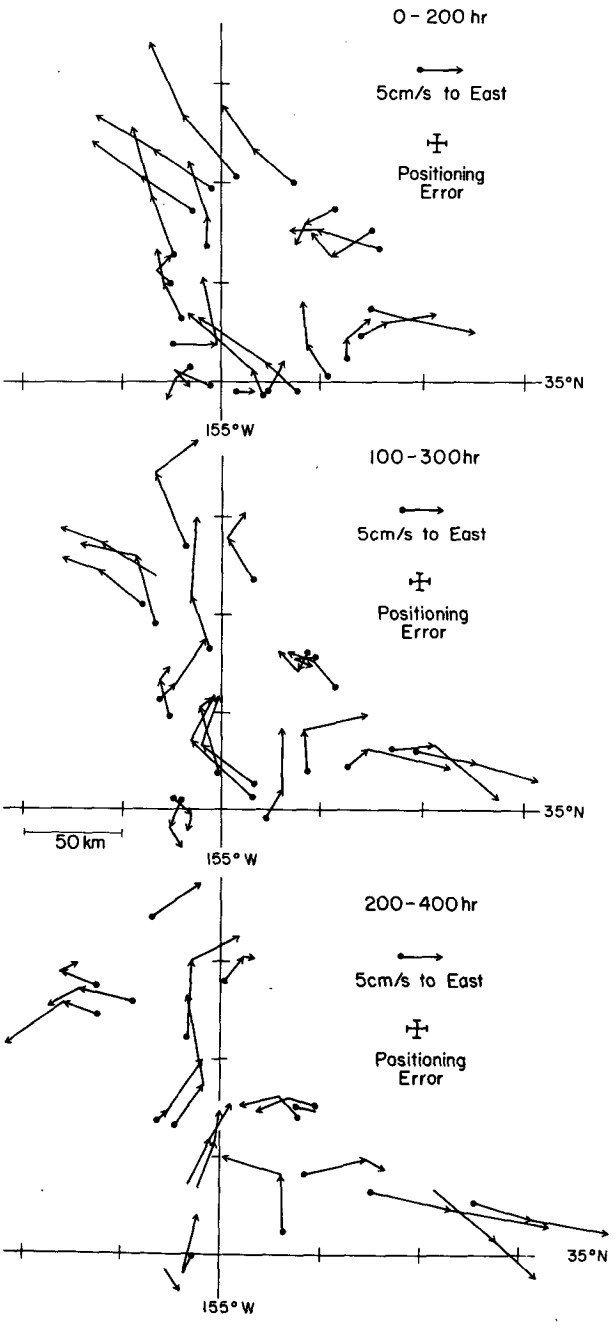

FIG. 6. Drifter position and velocity over 100 h periods. Time t = 0 corresponds to 0000 GMT 28 January 1974. Each panel depicts two overlapping 100 h periods. See Fig. B2 for estimates of wind-driven slippage errors.

Unauthenticated | Downloaded 06/20/24 10:10 PM UTC

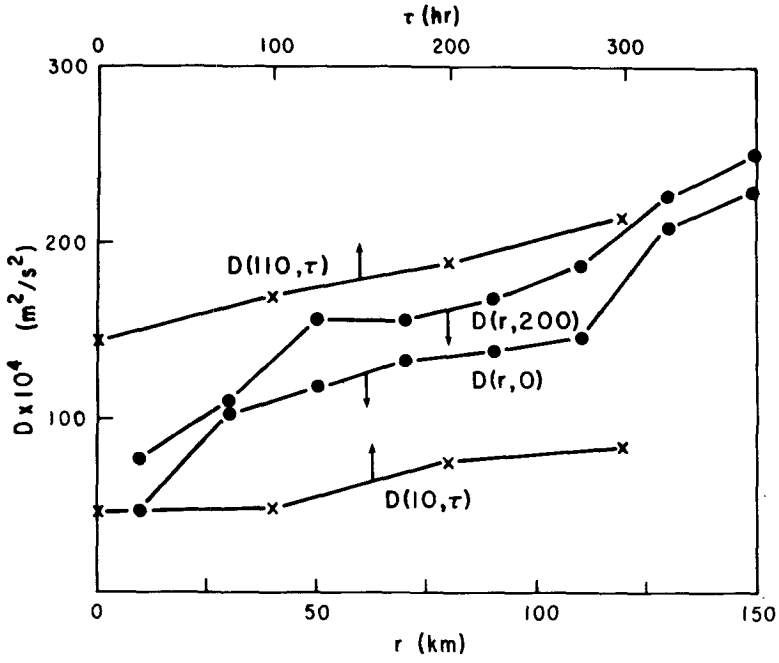

FIG. 7. Various cuts of the structure function $D(r,\tau)$ for drifter velocity. Shown are cuts along the τ axis holding r = 10 km and 110 km as well as cuts along the r axis holding τ = 0 and 200 h.

gives the viewer of Fig. 6 the impression of a straining motion (elongation) along the northwest-southeast axis.

The observed variability is not isotropic since the standard deviations for the eastward and northward velocities were $\sigma_1 = 0.05$ m s^{-1} and $\sigma_2 = 0.04$ m s^{-1}, respectively. That the scale content of the two components is similar is seen from the normalized structure function

$$\hat{D}_{ij}(r,\tau) = \frac{\langle [u_i(\mathbf{x}_1,t_1) - u_i(\mathbf{x}_2,t_2)][u_j(\mathbf{x}_1,t_1) - u_j(\mathbf{x}_2,t_2)]\rangle}{\sigma_i\sigma_j},$$

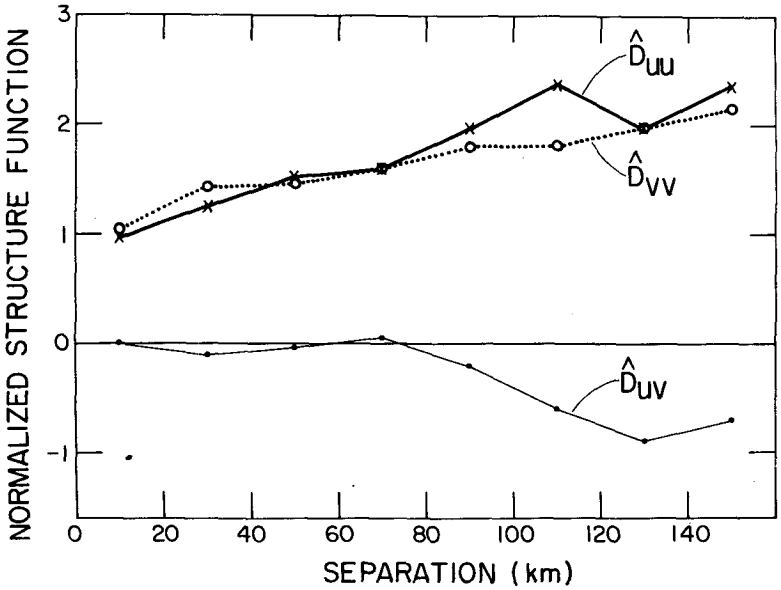

FIG. 8. The normalized structure functions from Eq. (3.2). When the difference between the mean-square velocities are accounted for the field appears to be isotropic.

Unauthenticated | Downloaded 06/20/24 10:10 PM UTC

where the averaging process is as described above and σ_i is the root mean square of the u_i component.

The essence of the above calculation is given in Fig. 8. The near constancy of flow field in time was used to average over all temporal separations less than 13 days thereby increasing the effective degrees of freedom associated with $\hat{D}$. The following conclusions may be drawn from the illustration:

4) The functions $\hat{D}_{uu}$ and $\hat{D}_{vv}$ are virtually identical indicating the normalized velocity components in the flow field have the same length scale dependence irrespective of the direction of flow. Similar calculations on other directional representations of the velocity field appear isotropic to first order.

5) The cross structure function $\hat{D}_{uv}$ is essentially zero out to separations of order 100 km.

In summary, conclusions 1–5 plus Figs. 7 and 8 combine to provide a crude model of the rms velocity associated with different scale ranges: Currents with unresolved small time and space scales have rms speeds of about 0.04 m s^{-1}. Currents with long time scales, but space scales of around 40 km have rms speeds around 0.07 m s^{-1} and there is additionally a large-scale field whose rms speed over the POLE region was about 0.05 m s^{-1}.

In an attempt to detect wind driven variability in the drifter field, the region was divided into geographical quadrants with approximately equal numbers of drifters in each. Mean currents were found for the quadrants and anomalous 100 h average currents obtained. The anomalies were typically of order 0.01–0.03 m s^{-1} and showed no significant correlation with 100 h average surface winds. This is not inconsistent with the *Flip* results which, when averaged over 100 h, also show no significant correlation in between wind and current. The apparent correlation of wind and current at *Flip* results from scales of variability badly aliased in the 100 h averages.

4. Sampling strategies

The profiling results indicate that, in the weak wind, deep mixed layer conditions encountered in POLE, there is little shear of low-frequency near-surface currents. If typical, these results would mean that a measurement strategy producing limited vertical resolution may be quite satisfactory in characterizing the low-frequency structure of the upper 100 m.

On the other hand, the relatively gradual decrease of energy with frequency observed in the profiler results points to the difficulty of resolving vertical structure of variability having time scales less than the inertial period. In order to prevent rather severe aliasing, it is necessary to sample extensively in time. Vertical profilers which sample each level only a few times in an inertial day do not yield a reliable picture of vertical structure in the presence of such vigorous high-frequency contamination.

The drogue program was designed to find that scale information required to properly plan a horizontal sampling scheme capable of resolving large-scale currents which may play a role in thermal anomaly dynamics. The requisite information is contained in the structure function D which we have sampled for time separations less than 20 days and space separations less than 150 km. We illustrate the sampling errors associated with such a field by determining the accuracy with which large scale currents could be mapped. Let $\mathbf{U}(x,t)$ be defined as the space/time average of the velocity $\mathbf{u}$ over a circular region of diameter 150 km and time span of 20 days centered at $\mathbf{x},t$. Each observation is $\mathbf{u}_n = \mathbf{U}(\mathbf{x},t) + \mathbf{u}'_n$ and an acceptable estimate is

$$\hat{\mathbf{U}} = \frac{1}{N} \sum \mathbf{u}_n.$$

We inquire how well the large-scale current $\mathbf{U}$ can be mapped.

The expected sampling error

$$\epsilon^2 = \langle |\mathbf{U} - \hat{\mathbf{U}}|^2 \rangle = \frac{1}{N^2} \sum_n \sum_m \langle \mathbf{u}'_n \mathbf{u}'_m \rangle \quad (4.1)$$

depends on the number of observations and the covariance of the various samples which, itself, is determined by the time and location at which observations are made. An efficient sampling scheme yields an acceptable error ϵ^2 for a minimum observation effort. If the noise were of very small time and space scales, then different observations would be uncorrelated, giving $\epsilon^2 = \langle |\mathbf{u}'|^2 \rangle / N$. But if the various observations are correlated, the error decreases more slowly than $1/N$, demonstrating that nearly redundant observations do little to average out noise. The noise covariance, which determines the efficiency of the sample scheme, is computable directly from the structure function D of (3.1).

For the POLE drogues the estimated eastward and northward mean currents were $\hat{U} = -2$ mm s^{-1} and $\hat{V} = 26$ mm s^{-1}, respectively. The *incorrect* sampling error estimate $\epsilon^2 = \langle |\mathbf{u}'|^2 \rangle / N$ gave $\epsilon = 7$ mm s^{-1} and the correct sampling estimate computed directly from (4.1) gave $\epsilon = 12$ mm s^{-1}, corresponding to about 33 independent observations rather than the 105 velocity samples actually taken.

If an accuracy of 10–20 mm s^{-1} is required in order to define the currents producing advective thermal anomalies, fairly extensive spatial sampling appears required. High-frequency variability and buoy positioning errors are reasonably well filtered out by intensive time sampling; positioning errors of the order a few kilometers add little to the noise coming from high-frequency natural variability and both are reasonably well-filtered by sampling about once

Unauthenticated | Downloaded 06/20/24 10:10 PM UTC

daily. The more significant noise comes from variability with long time scales and space scales of O(40 km) giving $D(r,0)$ and $D(r,200)$ of Fig. 7 their rapid increase from $r = 0$ to $r = 50$ km. For uniform buoy separation greater than O(30 km), N observations over the span of a week produce sampling errors of about $70/N^{1/2}$ [mm s^{-1}]. If the sampling is more dense the decrease with N is slower than $N^{-1/2}$. Thus 25 buoys in a region of the order 150 km on a side yield a 15 mm s^{-1} resolution; averaging over 30 days would reduce this to about 10 mm s^{-1}. If averages over larger spatial extents are desired, the error will, for a given number of buoys, exceed these estimates by an amount which cannot be estimated from our data.

5. Conclusions

The objectives of the POLE experiment were 1) to gather scale information necessary for the design of observational schemes to measure the processes believed important in the generation of large scale upper-ocean thermal anomalies, and 2) to investigate the dynamics pertinent to these processes to the extent possible.

With regard to sampling our conclusions are:

1) The high-energy content of current fluctuations, with periods less than a few hours (see Fig. 1), badly aliases infrequently sampled time series. Hence vertical profiling with a single instrument may not be adequate to resolve vertical structure with time scales less than a few days and use of moored strings of many meters is indicated.

2) The vertical structure of the observed low-frequency currents was simple, the entire layer above 135 m being highly coherent for frequencies <0.05 cph and very little veering with depth being evidenced. If this result is typical, it suggests that high vertical resolution of low-frequency currents is not required.

3) The drifter observations were subject to an apparent "noise" much larger than positioning errors. This is apparently due to small-scale or high-frequency currents. This suggests that positioning accuracy ceases to increase the utility of drifter inferred velocity when the velocity errors associated with positioning are on the order of 0.05 m s^{-1} [see conclusion 1 of Section 3].

4) In addition to the above unresolved "noise", the drifters disclosed a signal of small spatial scale (of the order 40 km) but unresolvably long time scale (>15 days) with rms velocities of the order 0.07 m s^{-1}. This too serves as noise to the observation of large scale currents. Suppression of this noise is inefficient for observations more closely separated than O(30 km), and nothing is gained by sampling more frequently than once every few days at the same location. This signal may well be the surface manifestation of mesoscale eddies as found in MODE-I.

5) The POLE results are inadequate to fully assess the difficulty of measuring very large-scale currents since they do not characterize the largest scale variability. The need to filter the mesoscale variability found in POLE gives a lower bound on the accuracy of any given observing array and this may well be the most difficult problem in observing currents on a climatically significant scale.

With regard to dynamics, our conclusions are:

6) Current meter profiling disclosed currents of subinertial frequencies and large vertical scale which appear coherent with and parallel to the local wind stress. This variability was much too energetic to be directly forced by the local wind. The drifters show no evidence of displacements over 100 h intervals being correlated with the wind but this period is rather long compared to the time scale of the wind stress. It is possible that the apparent coherence with the wind is spurious; the statistical reliability is low. It is possible that the currents are generated by nearby winds much stronger than those observed but this conjecture receives no support from any available dynamical model. An interesting possibility, provided by Dr. Rory Thompson (private communication), is that *Flip*, being a drifting body, seeks out locations in the flow where there is an anomalous downwind current. For example, in an eddy field consisting of rolls with axes parallel to the wind, *Flip* would tend to collect at a convergence zone where the vertical eddy velocity is downward. If the Reynolds stress $\langle w'\mathbf{u}'_H\rangle$ transfers downward momentum parallel to the wind, then *Flip* would favor a position where the turbulent velocity $\mathbf{u}'_H$ tends to be in the direction of the wind and would be found less frequently in the regions of the rolls where w' is up and $\mathbf{u}'_H$ tends to be antiparallel to the wind. Thus even though $\langle\mathbf{u}'_H\rangle = 0$ a drifting body might tend to sample selectively the positions where $\mathbf{u}'_H$ is directed downwind.

7) The large-scale surface currents, as best we could determine them, were very small (~0.02 m s^{-1}) as compared with what is normally accepted as a climatological norm for the season and location [the surface current derived from ship drift is of the order 0.15 m s^{-1} to the southeast (U. S. Hydrographic Office, 1961)]. Either the ship drift charts are extremely unreliable or there are very large variations of near surface currents occurring over large areas and persisting for periods of the order one month. If the latter is true, the possibility of thermal anomalies generated by advection is great. It takes but 0.03 m s^{-1} across the climatologically normal horizontal temperature

Unauthenticated | Downloaded 06/20/24 10:10 PM UTC

gradient [($\sim$1°C (100 km)$^{-1}$] to generate a 1.0°C anomaly in one month.

8) There existed in the POLE region an energetic mesoscale variability of near-surface currents having speeds of O(0.07 m s^{-1}), space scales of O(40 km) and time scales in excess of 20 days. The dynamics of these motions is not understood. Future comparison of velocity and density observations made during the experiment may shed light on this question.

APPENDIX A

The Profiling System

The profiling current meter consisted of three Bendix B-10 ducted propeller sensors aligned in the horizontal plane at angles of 120° from each other. The Bendix sensors were laboratory tested to determine their response to steady flow as a function of speed and angle between the flow and the sensor axis. The stall speed was found to be approximately 25 mm s^{-1} and the response linear above 40 mm s^{-1}. The angular response was disappointingly different from the ideal of a $\cos\theta$ law. The response was generally higher than $\cos\theta$ for $10° < \theta < 30°$ by up to 10%, approximately correct for $20° < \theta < 50°$, and then dropped to zero response at about 70°. It was this lack of response at high angles which led to the use of three, rather than two, sensors to observe the horizontal velocity. In operation, the two sensors with largest readings over a 2 s interval were used to define the current.

The choice of propeller sensors, rather than the more conventional rotor and vane combination, was dictated by a desire to eliminate rectification of surface wave motion and vibration of the meter caused by dynamic forces on the suspending cable; Gould and Sambuco (1975) have shown that such high-frequency signals can be rectified by rotor and vane meters to produce significant errors. To test if the sensors employed were subject to rectification they were placed at the center of a wave tank in the presence of waves of 0.7 m height and 6 s period, 0.4 m height and period 4 s, and 0.2 m height and 2 s period. The meter was rotated through 360° in 30° steps with readings recorded in each orientation. No absolute velocity reference was available against which to compare the propeller sensors and the difference between Eulerian and Lagrangian mean currents precluded use of dye tracing to infer mean Eulerian current. Confidence that the sensor did not rectify the wave signals was provided by the fact that, in orbital speeds of the order 0.30 m s^{-1}, the mean current inferred from the sensor was repeatable between different runs and consistent with the steady flow calibration for each orientation to within 10 mm s^{-1} with a mean square error of less than 5 mm s^{-1}. Work is presently underway to develop a better propeller sensor, capable of a true cosine response, and to provide a more satisfactory method of dynamic testing.

In operation the three sensors were mounted, together with a small pressure case housing electronics and a compass, in a tetrahedron about 1.3 m on a side. The entire package was lowered from a boom 25 m distant from *Flip*'s axis. Neither *Flip*'s hull nor the 40 kg depressing weight suspended 5 m below produced detectable compass deviation. *Flip*'s motion is limited to periods > 15 s; the heave amplitude is typically less than 0.2 m (Rudnick, 1967). The diameter of *Flip* is 4 m near the surface and 6.5 m over the lower 70% of its 100 m draft. No detectable inclination (<3°) of the meter's suspending cable was observed so the meter was at least three diameters from *Flip*'s axis.

The profiling meter measured water velocity relative to *Flip* which was freely drifting. The drift of *Flip* was determined from satellite fixes with an average frequency of one good fix every 1.5 h and occasional gaps of up to 4 h. The inertial navigation equipment intended to interpolate motion between fixes failed to operate. A continuous estimation of *Flip* velocity was constructed using an unbiased minimum expected square error statistical estimator (Leibelt, 1967). The structure function

$$\langle[\mathbf{X}(t) - \mathbf{X}(t + \tau)]^2\rangle$$

of position $\mathbf{X}$ was least-squares fit to the form

$$\langle u^2\rangle\tau^2 + \langle e^2\rangle$$

for lags τ up to 5 h. The mean-square velocity $\langle u^2\rangle$ was found to be (0.13 m s^{-1})^2 and the mean-square noise $\langle e^2\rangle$ to be (220 m)^2. It was assumed that $\langle e^2\rangle$ represented noise in the satellite fixes and a minimum square error estimate of *Flip* velocity was constructed under this assumption. Regardless of the precise nature of $\langle e^2\rangle$, the rms error of 1 h averages of *Flip* velocity is approximately 20 mm s^{-1} and has an approximate frequency^{-1} spectrum below 1 cph (so that 10 h averages have an rms error of $\sim$4 mm s^{-1}).

The wind speed and direction from an anemometer at 25 m elevation were recorded at $\sim$1 h intervals. These readings were converted to wind stress using a quadratic law with a drag coefficient of 0.0015. A continuous record of wind stress was constructed using a minimum square error estimation algorithm similar to that employed to estimate *Flip* velocity; aliasing of this series is much less severe than the aliasing of relative velocity records obtained by occupying various depth levels with a single current meter.

Unauthenticated | Downloaded 06/20/24 10:10 PM UTC

APPENDIX B

The Drogued Drifters

Freely drifting buoys equipped with radio beacons and drogued at 30 m depth were tracked by aircraft. Twenty-six buoys were deployed, 25 operated satisfactorily for the duration of the experiment. The aircraft made a total of 11 flights of which four were dedicated solely to buoy positioning and some buoy positioning was also accomplished during the others. On the average, each of the 25 buoys was positioned from 4–6 times during the 21-day experiment. The following paragraphs describe buoy characteristics, methods of positioning and system errors.

The buoy system, shown schematically in Fig. B1, consisted of a transmitter buoy containing electronics and power, a flotation buoy and an approximately 8 m diameter parachute drogue. The transmitter, for location, was contained in a 1.1 m × 0.15 m tube with 5.5 kg ballast for righting and net buoyancy of 2.7 kg. The main flotation was a separate 0.6 m vinyl float tethered to the transmitter buoy by a nylon line; a PVC pipe was lashed to this line, preventing fouling. The two-part buoy allowed a small surface buoyancy float which might be temporarily submerged while the transmitter antenna remained above the surface.

The VHF transmitters were Navy issue SSQ41A sonobuoy transmitters with scuttle circuits removed and voltage regulation added to insure stable transmission frequency. The standard sonobuoy antenna was duplicated from plastic and stainless steel to insure adequate life. The transmission frequency was modulated for buoy identification and transmitters carefully tuned for maximum output (an important detail). Transmission power was switched from 0.8 to 2.0 W allowing reception at ranges up to 150 nm by an aircraft at 20 000 ft altitude and a battery life exceeding 20 days.

The buoys were positioned using the VHF radio direction finder aboard the NAVOCEANO P-3A used during the experiment. Initial reception and crude positioning of buoys was made from 20 000 ft altitude. Precise positions were determined by homing on the buoy and noting the aircraft position at the time of RDF needle reversal. The primary position errors result from inaccuracies of the inertial navigation system employed (an LTN-51). The system was initialized by overflying *Flip* (which had satellite navigation) before and after a buoy run. Overall positioning error is estimated as 1 n mi.

The drag elements were 8 m diameter cargo parachutes, tethered on 30 m of line and held at depth by a 16 kg weight. One of the drogues was recovered at the experiment's end; the parachute was fouled. To estimate buoy slippage from wind drag some laboratory tests were carried out. Wind drag was computed using a quadratic drag law and projected areas for the transmitter float, antenna and main float all with $C_D = 1$. The drag of an open parachute was similarly computed assuming

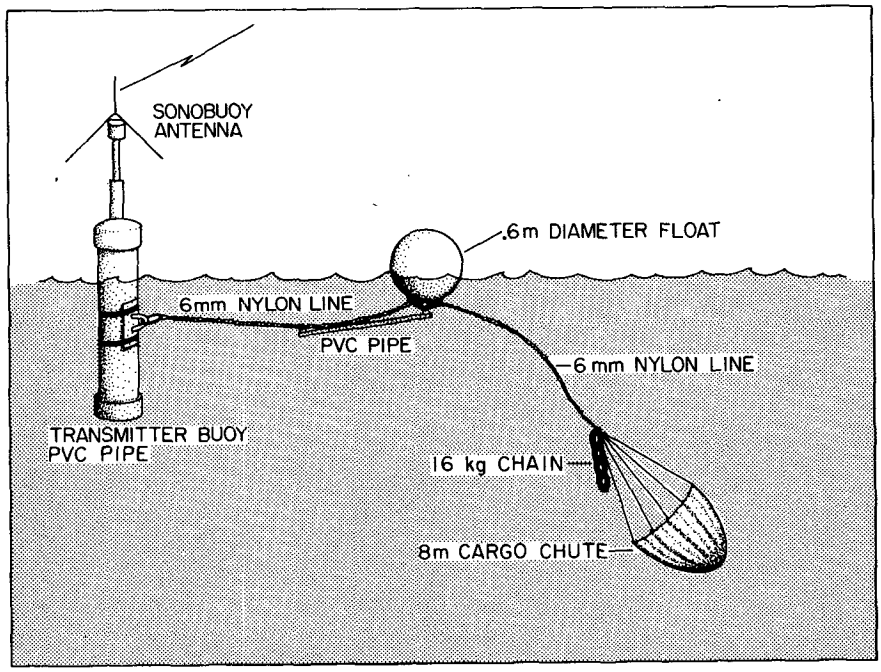

FIG. B1. Schematic drifter system. See text for description and function of the various components.

Unauthenticated | Downloaded 06/20/24 10:10 PM UTC

$C_D = 1$. The drag of a fouled parachute was measured by tying a parachute into a small bundle (much smaller than a naturally fouled parachute) and towing it. The resulting drag was consistent with a quadratic drag law, $C_D = 1$, and an area 1/400 of the unfouled parachute. Assuming the buoy drag was determined by the wind speed at 0.25 m and that the profile is logarithmic with a roughness length of 20 mm leads to a linear relation between drift velocity u and wind speed at 25 m of

$$u = \alpha U_{25} \tag{B1}$$

with $\alpha = 0.8 \times 10^{-2}$ for a fouled drogue and $\alpha = 0.4 \times 10^{-3}$ for an open drogue.

The net buoy drift was computed from (B1) and observed winds. The results (Fig. B2) show a net northeasterly drift over the course of the experiment. For fully open parachutes, the drift over 17 days is 1.8 km; for fully fouled, it is 36 km. Even the pessimistic estimate of fully fouled drogues is only 20% of the typical buoy drift over this period.

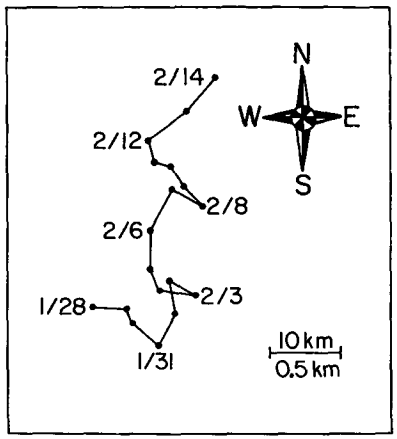

FIG. B2. Estimated wind-induced buoy drift. The 10 km scale is appropriate for completely fouled drogues, the 0.5 km scale for open drogues.

Acknowledgments. The crew of the NAVOCEANO P-3 and the NAVOCEANO liaison team, headed by Jeff Kerling, were of great help in the Aircraft Program. Meredith Sessions and Steve Rearwin, both of SIO, played vital roles in the airborne data recording and gathering activities. Bill Johnson, Jack Lucas and the late Wayne Hill of SIO built and deployed the surface drifters and the profiling current meter. This research was sponsored by the Office of Naval Research under Contract N00014-69-A-0200/6043.

REFERENCES

Barnett, T. P., 1976: Interannual changes in the thermal structure of the central Pacific Ocean. *Trans. Amer. Geophys. Union*, **57**, 942.

Bretherton, F. B., R. E. Davis, and C. B. Fandry, 1976: A technique for objective analysis and design of oceanographic experiments as applied to MODE-73. *Deep-Sea Res.*, **23**, 559–582.

Davis, R. E., 1976: Predictability of sea surface temperature and sea level pressure anomalies over the North Pacific Ocean. *J. Phys. Oceanogr.*, **6**, 249–266.

Gonella, Joseph, 1972: A rotary-component method for analyzing meteorological and oceanographic vector time series. *Deep-Sea Res.*, **19**, 833–846.

Gould, W. J., and E. Sambuco, 1975: The effect of mooring type on measured values of ocean currents. *Deep-Sea Res.*, **22**, 55–62.

Jenkins, G. M., and D. G. Watts, 1968: *Spectral Analysis and Its Applications*. Holden-Day, 523 pp.

Liebelt, P. B., 1967: *An Introduction to Optimal Estimation*. Addison-Wesley, 253 pp.

Namias, J., 1970: Macroscale variations in sea surface temperatures in the North Pacific. *J. Geophys. Res.*, **75**, 564–581.

Rudnick, P., 1967. Motion of a large spar buoy in sea waves. *J. Ship. Res.*, **11**, 257–267.

U. S. Hydrographic Office, 1961: *Climatological and Oceanographic Atlas for Mariners*, Vol. 2, *North Pacific Ocean*, 159 pp.

White, W. B., and A. E. Walker, 1974: Time and depth scales of anomalous sub-surface temperature at Ocean Weather Stations P, N and V in the North Pacific. *J. Geophys. Res.*, **79**, 4517–4522.

Unauthenticated | Downloaded 06/20/24 10:10 PM UTC